Cite this: *J. Mater. Chem. A*, 2020, **8**, 1808

An *in situ* structural study on the synthesis and decomposition of $LiNiO_2$†

Matteo Bianchini, *[a] François Fauth, [b] Pascal Hartmann,[ac] Torsten Brezesinski [a] and Jürgen Janek *[ad]

DOI: 10.1039/c9ta12073d

The electrification trend in the automotive industry is fueling research on positive electrode materials with high specific capacities. The nickel content in such layered oxide systems is continuously increasing, and so is the importance of $LiNiO_2$ (LNO). Despite decades of research, LNO still exhibits properties, closely related to its instability, that require better understanding. One of these is the difficult solid-state synthesis that never seems to yield LNO samples of perfect stoichiometry. At present, improved experimental capabilities allow for investigating the synthesis process in unprecedented detail. Here, we leverage synchrotron X-ray diffraction, carried out *in situ* during calcination and decomposition of LNO at high temperature, to reveal the evolution of precursor materials during solid-state synthesis. We evaluate the effect of pre-annealing the hydroxide precursors' mixture at low temperature, prior to the actual calcination at 700 °C. We then show that LNO formation is a structurally complex process, beginning from LNO seeds with a compressed rhombohedral unit cell (c/a < 4.9) within the rock salt framework. We identify a key aspect in the presence of Ni vacancies in Ni slabs, creating space for cation migration and allowing for the material's layering. We also investigate the decomposition of LNO, since it can be seen as the reverse process of synthesis. In fact, beginning already at 700 °C, it is in a way a byproduct of the synthesis. We correlate the change in stoichiometry with the unit cell volume of LNO and show how permanent damage is done to it by even a short time at too low O_2 chemical potential. Taken together, this work aims at providing insights that may be of help in optimizing the synthesis of LNO while minimizing decomposition effects. Moreover, the same information can be seen as a starting point to further studies on Ni-rich (doped) compositions of practical interest.

Introduction

$LiNiO_2$ (LNO) is one of the best known, but likely most complicated, positive electrode materials for Li-ion batteries.[1] Since its introduction in 1990,[2] many efforts have been made towards the reduction of Ni content by substitution with other elements, leading to the development of NCM (nickel–cobalt–manganese) and NCA (nickel–cobalt–aluminum) oxide cathode materials. These compounds exhibit greater electrochemical stability (in terms of long-term cycling and safety) when cycled at moderate cut-off voltages, which, however, comes at the price of limiting their gravimetric capacity.[3,4] Yet, more recently, the need for more energy-dense batteries for automotive applications has fueled a trend to re-increase the Ni content, with the goal of boosting gravimetric capacity, ultimately exploring compositions with ≥95% Ni.[5–7] Overall, this is a difficult task due to the challenges posed by Ni-rich compositions, and eventually by LNO. A well-known trade-off between capacity and stability exists in both NCM and NCA cathode materials (and thus in LNO) and is tackled by academia and industry alike.[3,8–10]

Here, we only highlight a few points on LNO relevant to the present study; for a more extensive discussion we direct the reader to a recent review of the large body of scientific literature on this material.[1] LNO is a layered oxide built on a cubic close packed array of oxygen ions, as depicted in Fig. 1; Ni and Li atoms are arranged in edge-sharing octahedral environments and are alternated along the c axis of the rhombohedral unit cell. The main driving force for layering and inducing a rhombohedral distortion of the parent cubic lattice is the different size of Li^+ and Ni^{3+} ($r(Li^+) = 0.76$ Å and $r(Ni^{3+}) = 0.56$ Å (ref. 11)), the latter being oxidized from Ni^{2+} in the precursor [*e.g.*, $Ni(OH)_2$] during calcination in oxygen-containing atmosphere. Challenging for the application of LNO in a battery is its intrinsic structural instability, both in the pristine state and in

[a]*Battery and Electrochemistry Laboratory, Institute of Nanotechnology, Karlsruhe Institute of Technology (KIT), Hermann von Helmholtz Platz 1, 76344 Eggenstein Leopoldshafen, Germany. E mail: matteo.bianchini@kit.edu*

[b]*CELLS ALBA Synchrotron, Cerdanyola del Vallès, 08290 Barcelona, Spain*

[c]*BASF SE, Carl Bosch Strasse 38, 67056 Ludwigshafen, Germany*

[d]*Institute of Physical Chemistry & Center for Materials Science (ZfM/LaMa), Justus Liebig University Giessen, Heinrich Buff Ring 17, 35392 Giessen, Germany. E mail: Juergen.Janek@phys.Chemie.uni giessen.de*

† Electronic supplementary information (ESI) available. See DOI: 10.1039/c9ta12073d

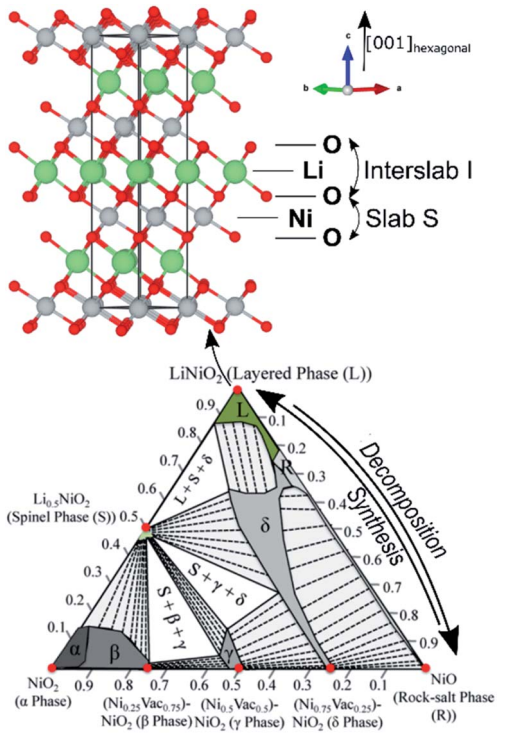

Fig. 1 NiO $LiNiO_2$ NiO_2 finite-temperature phase diagram computed by Das *et al.* at 1 atm, 600 K. Synthesis and decomposition of LNO are processes occurring along the NiO $LiNiO_2$ side of the triangle. Adapted with permission from Das *et al.*,[12] Copyright 2017 American Chemical Society. The crystal structure of layered $LiNiO_2$ is shown on top. Green spheres represent lithium, grey ones nickel, and red ones oxygen.

the delithiated state reached upon electrochemical cycling. In this work, we addressed the former and studied the structural properties of pristine LNO in real time (*in situ*) during synthesis and decomposition processes.

The complexity of LNO's synthesis results from its peculiar position in the Li_2O–NiO–O_2 phase diagram, a section of which is reported in Fig. 1. LNO is part of the $Li_{1-y}Ni_yO$ solid solution of compositions $(1/3 \leq y \leq 1)$.[1] The value of 1 y (the amount of Li that can be incorporated) determines the crystal structure (from cubic to rhombohedral to monoclinic as y decreases) and is a function of the oxygen chemical potential $\mu(O_2)$. Any displacement of the target stoichiometry from the intended one, or any unintended variation of the $\mu(O_2)$ during synthesis (*i.e.*, more/less oxidative environment), can move the reaction equilibrium towards a different product, a defective LNO. The most common of such products, called off-stoichiometric, is almost ubiquitous in literature and is the result of Li loss during annealing and the difficulty to fully oxidize Ni to the trivalent state. It can be written as $Li_{1-z}Ni_{1+z}O_2$ (representing the NiO–$LiNiO_2$ tie line in Fig. 1). Note that the phase diagram of Fig. 1 was obtained from computations, while experimental ones have also been reported in the literature.[13,14]

LNO is barely stable in its pristine state (not to mention the delithiated states).[1] As a result, during calcination Li can be lost from the phase, accompanied by oxygen loss[15] and by formation of a rock salt-type phase, often reported in TEM studies of LNO[16] and related nickel-rich oxides.[17] The decomposition (Fig. 1) is believed to mostly affect the surface region of the material.[18] It proceeds according to:

$$LiNiO_2 \rightarrow \frac{1}{1+z}Li_{1-z}Ni_{1+z}O_2 + \frac{z}{1+z}Li_2O + \frac{z}{2(1+z)}O_2 \quad (1)$$

and can be seen as the reverse of the synthesis process (which would have a leftwards arrow and start from $z = 1$). The presence of Li_2O among the decomposition products is supported by thermogravimetric analysis (TGA) and X-ray diffraction (XRD) studies,[19,20] although its observation is difficult because, in an atmosphere containing O_2, Li_2O reportedly reacts to form volatile Li_2O_2.

Note that one can write LNO as $LiNiO_2$, as is usually done, or as $Li_{0.5}Ni_{0.5}O$, which better reflects its relationship with the parent NiO rock salt-type phase. It is simply a matter of convention. In the following, we will mostly use the common convention: we write phases possessing a layered structure as $Li_{1-z}Ni_{1+z}O_2$ and phases possessing a rock salt-like structure as $Li_{1-y}Ni_yO$. In some cases, the subscript C for cubic and R for rhombohedral is added for clarity.

For the reasons described above, in this work we proceed to a detailed *in situ* synchrotron X-ray diffraction study of the synthesis and decomposition of $LiNiO_2$. Thanks to their real-time nature, *in situ* synthesis XRD experiments are powerful tools to investigate reaction pathways and in particular the relative importance of kinetic and thermodynamic aspects.[21] By achieving high angular and time resolution, we aim at obtaining new insights into the structural evolution and kinetics of lithiation/oxidation of rock salt-type NiO and into the opposite process resulting in oxygen and lithium loss from LNO.

Methods

The details of a typical $LiNiO_2$ synthesis, such as the one used to prepare the material for the decomposition study, and the morphology of the product, have been reported elsewhere.[15] Briefly, $Ni(OH)_2$ and $LiOH \cdot H_2O$ (BASF) were used as precursors. The materials were mixed and heated in an alumina crucible at 700 °C for 6 h. The process was carried out in a tubular furnace in a stream of pure oxygen gas.

The synchrotron XRD experiments were carried out on the MSPD beamline of the ALBA synchrotron.[22] Two different synthesis reactions were investigated *in situ*. The first used analogous precursors to the above-described one, in a 1 : 1.01 ratio. In the second one, the nickel and lithium hydroxides were mixed and heated beforehand at 350 °C for 12 h (pre-annealing). This process typically results in a mixture of NiO and LiOH, as confirmed by TGA and XRD (Fig. 2 and S1 in ESI†). In both cases, a quartz capillary of 1 mm in diameter open on both ends was filled with the powder mixture and mounted on a custom support (a so-called capillary flow cell[23]). The cell allows placing the capillary in the center of the diffractometer goniometer, whilst flowing a stream of pure oxygen gas through the capillary (Fig. S2†). Furthermore, the whole setup was rocking by ±5° around the goniometer center to improve

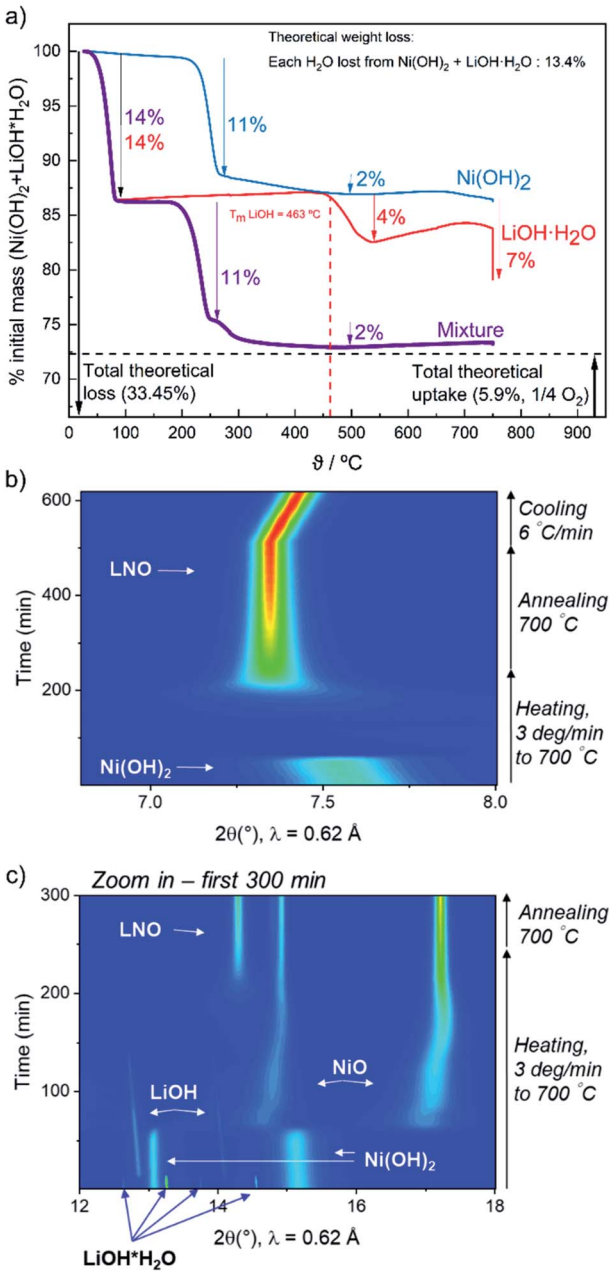

Fig. 2 (a) Thermogravimetric analysis of $Ni(OH)_2$ (green), $LiOH \cdot H_2O$ (red) and precursor mixture for the synthesis of LNO [*i.e.*, $Ni(OH)_2$ + $LiOH \cdot H_2O$] (violet). Heating rate is 3 °C min ^{1}. For all samples, the % written is referring to the initial stoichiometry of $Ni(OH)_2$ + $LiOH \cdot H_2O$ (total molecular weight 134.67 g mol ^{1}), thus, *e.g.*, the loss of one H_2O implies a weight loss of 13.4%. (b and c) *In situ* synchrotron X-ray diffraction during synthesis of $LiNiO_2$ from a mixture of $Ni(OH)_2$ and $LiOH \cdot H_2O$. The contour plots (2θ regions 6.5 8° (b), 12 18° (c)) show the evolution of Bragg reflections during heating. (b) Shows the whole experiment, (c) only the first 300 minutes.

powder averaging over multiple crystallites. The capillary was heated using a hot air-blower (FMB Oxford) placed right above it. The temperature scale at the hot-blower tip (where a thermocouple is placed) had been previously calibrated at the beamline using the thermal expansion of Si powder as reference.

Diffraction data were collected using the one-dimensional silicon-based position-sensitive detector MYTHEN in Debye–Scherrer geometry in 2θ angular range of 2–55° (d-range: 0.7–15 Å). For synthesis experiments, the wavelength was set at $\lambda = 0.6194$ Å, calibrated using a Si NIST standard sample. The acquisition time was 1 min for all XRD experiments. Since MYTHEN detector spans a ~40° angular 2θ range, this setup allows fast data acquisition with extremely high statistics and good angular resolution. A typical full width at half-maximum (FWHM) for representative peaks of LNO obtained during the *in situ* synthesis is 0.07° [(003) at $2\theta = 7.44°$] and 0.08° [(104) at $2\theta = 17.38°$]. The instrumental contribution to the peak broadening was obtained by measuring a $Na_2Ca_3Al_2F_{14}$ (NAC) sample as line broadening reference. The quality of the data collected in these conditions allows reliable Rietveld[24] structural refinements of the involved crystalline phases[25] using the FullProf software.[26]

For studying the decomposition of $LiNiO_2$, a pristine LNO powder had been prepared beforehand using the above-described synthesis method (Fig. S3†). A quartz capillary open on both ends was filled with the powder and XRD data were collected in air as a function of temperature. During the decomposition experiment, the overall conditions were similar as described above but the wavelength was set to $\lambda = 0.4130$ Å.

Results and discussion

(I) Solid-state synthesis of $LiNiO_2$

As mentioned in the methods section, we studied two different synthesis routes separately. First, starting from the pure hydroxides, $Ni(OH)_2$ and $LiOH \cdot H_2O$, and directly annealing them. Secondly, pre-annealing beforehand their mixture at 350 °C. In the latter case, as verified also by TGA (Fig. 2), the following reaction occurs:

$$Ni(OH)_2 + LiOH \cdot H_2O \rightarrow NiO + LiOH + 2H_2O \quad (2)$$

So one expects to obtain a NiO and LiOH precursor mixture. Since we want to focus on the formation of LNO, occurring above 350 °C, only the latter synthesis is discussed in the following. Moreover, the synthesis starting from the hydroxides is less suitable for detailed Rietveld refinement analysis because of the significant volume loss due to water evaporation, leading to poor capillary filling. The experimental data for the synthesis starting from the hydroxides are nonetheless shown in Fig. 2 and S4.† No major difference above 350 °C is seen between the two experiments. One should note the disappearance of the layered structure of $Ni(OH)_2$, with concurrent appearance of NiO (Fig. 2b and c). This allows to rule out the possibility of a topotactic H/Li exchange in the Ni system, contrary to what some authors suggested for the Co system, where $LiCoO_2$ can be directly synthesized at low temperature starting from $Co(OH)_2$.[27]

The combined lithiation and oxidation of the binary rock salt-like compound NiO was studied in real time by *in situ* synchrotron XRD. Fig. 3 shows the evolution of the main Bragg peaks during heating and annealing. The expected reaction from the pre-annealed precursors is:

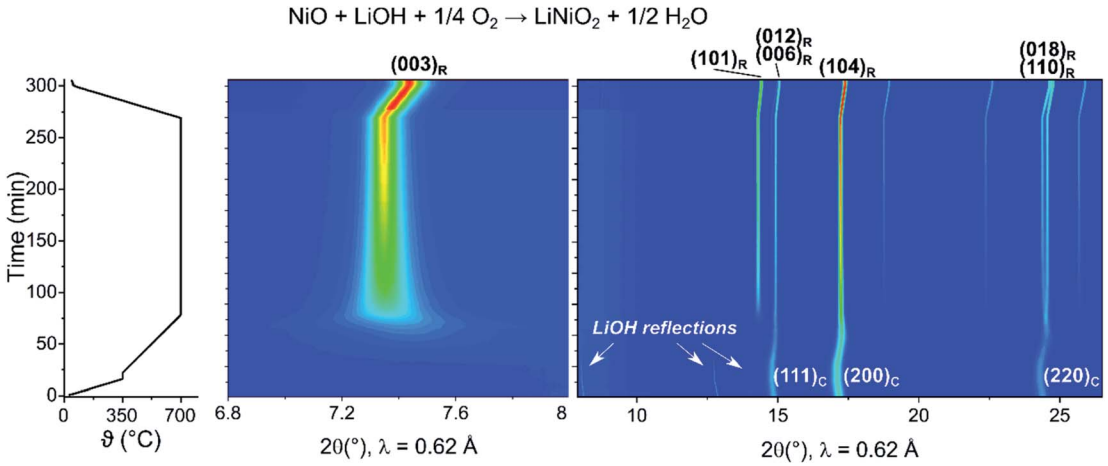

Fig. 3 *In situ* synchrotron X-ray diffraction during the synthesis of $LiNiO_2$ from a mixture of NiO and LiOH (made by pre-annealing the starting materials, $Ni(OH)_2$ and $LiOH{\cdot}H_2O$). (Left) Temperature evolution over time. (Middle and right) Contour plots showing the evolution of Bragg peaks during synthesis.

$$[NiO]_C + LiOH + \frac{1}{4}O_2 \rightarrow 2[Li_{0.5}Ni_{0.5}O]_R + \frac{1}{2}H_2O = LiNiO_2 + \frac{1}{2}H_2O \quad (3)$$

The peaks of LiOH disappear rapidly starting from $\vartheta \approx 430$ °C until $\vartheta \approx 492$ °C. Considering that the melting point of the compound is tabulated as $\vartheta_m = 446$ °C,[28] this serves as an indication of good temperature calibration in our experiment.

Since lithiated rock salt-type oxides can be prepared with compositions up to $Li_{0.3}Ni_{0.7}O$,[29,30] one can expect the formation of $LiNiO_2$ from NiO to occur in two steps. First, a "mixing" period, where Li homogenously distributes within the Ni sublattice up to a 30% Li : 70% Ni ratio, followed by a "layering" one, where Li^+ and Ni^{3+} segregate to reduce the steric constraints and induce a rhombohedral distortion of the original cubic lattice. In each step, both lithium and oxygen must be incorporated into the original rock salt-like lattice. The appearance of the $(003)_R$ peak is a clear indication for the onset of layering (Fig. 3). Another characteristic feature of the LNO XRD pattern is the splitting of some peaks [*e.g.*, $(220)_C$ becomes $(018)_R$ and $(110)_R$] due to the rhombohedral distortion. Some Bragg peaks on the other hand are maintained upon LNO crystallization due to the preservation of O stacking (*e.g.*, $(111)_C$ becomes $(006)_R$, but the two represent the same interplanar spacing $d \approx 2.38$ Å). One should note that we did not observe any oxidized nickel oxide, contrary to a recent report suggesting the presence of a Ni_8O_{10} phase (whose diffraction pattern would be indistinguishable from a lithiated rock salt phase).[31] We also did not experimentally observe specific intermediate phases $Li_{1-y}Ni_yO$ at $y = 2/3$, 5/6, 7/8 and 11/12, that are predicted to be stable at 0 K but are destabilized at typical synthesis temperatures in favor of a solid solution behavior, in agreement with *ab initio* phase diagrams.[12] In fact, no weak superstructure reflections could be identified in the background of our diffraction data, while we observe a continuum of compositions $Li_{1-y}Ni_yO$ for $0 < y < 0.5$, with a cubic to rhombohedral phase transition occurring close to $y \approx 0.6$.

Rietveld refinement of XRD data yields detailed information on the evolution and structural features of each phase. Fig. 4 gathers refined diffraction patterns at selected times during the early stages of the synthesis. Fig. 5, 6 and 7 highlight instead structural parameters derived from the refinement. Details on the refinement procedure including figure of merits are given in ESI (Fig. S5†). From Fig. 4, one can obtain a general idea of the refinement quality, evolution, and criticalities. At the beginning of the experiment, on top of a background whose shape is dominated by the contribution of the quartz glass capillary, one can see narrow peaks belonging to well-crystallized LiOH and broad peaks belonging to a cubic NiO-like phase (average apparent crystallite size 11 nm). As described in the next paragraph, this NiO-like phase is already a lithium-containing $Li_{1-y}Ni_yO$ rock salt phase. After 47 min, LiOH has almost entirely disappeared, while broad reflections mark the appearance of LNO, which then continuously decrease in width and grow in intensity over time. From the shape of LNO's Bragg peaks, it is possible to see that they are anisotropic in width [*e.g.*, $(101)_R$ at 14.3° is very broad, while the peak at 15° is narrow, despite belonging to overlapped $(006)_R$, $(012)_R$, and $(111)_C$].

To rationalize why only certain peaks are broad, LNO samples were synthesized at temperatures as low as 550 °C (12 h annealing time), exhibiting the same peak broadening (Fig. S6†). We find that the XRD pattern of these samples can be only fitted if a special anisotropic size broadening rule is used, namely $l = 2n + 1$ with $n = 0, 1, 2, \ldots$. In other words, Bragg reflections with odd I Miller index are broad, while even ones are narrow. The reason for such behavior can be found in the matrix transforming cubic Miller indices into rhombohedral ones:

$$\begin{bmatrix} h \\ k \\ l \end{bmatrix}_{LNO} = \begin{bmatrix} 1/2 & 1/2 & 0 \\ 0 & 1/2 & 1/2 \\ 2 & 2 & 2 \end{bmatrix} \begin{bmatrix} h \\ k \\ l \end{bmatrix}_{rock\ salt}$$

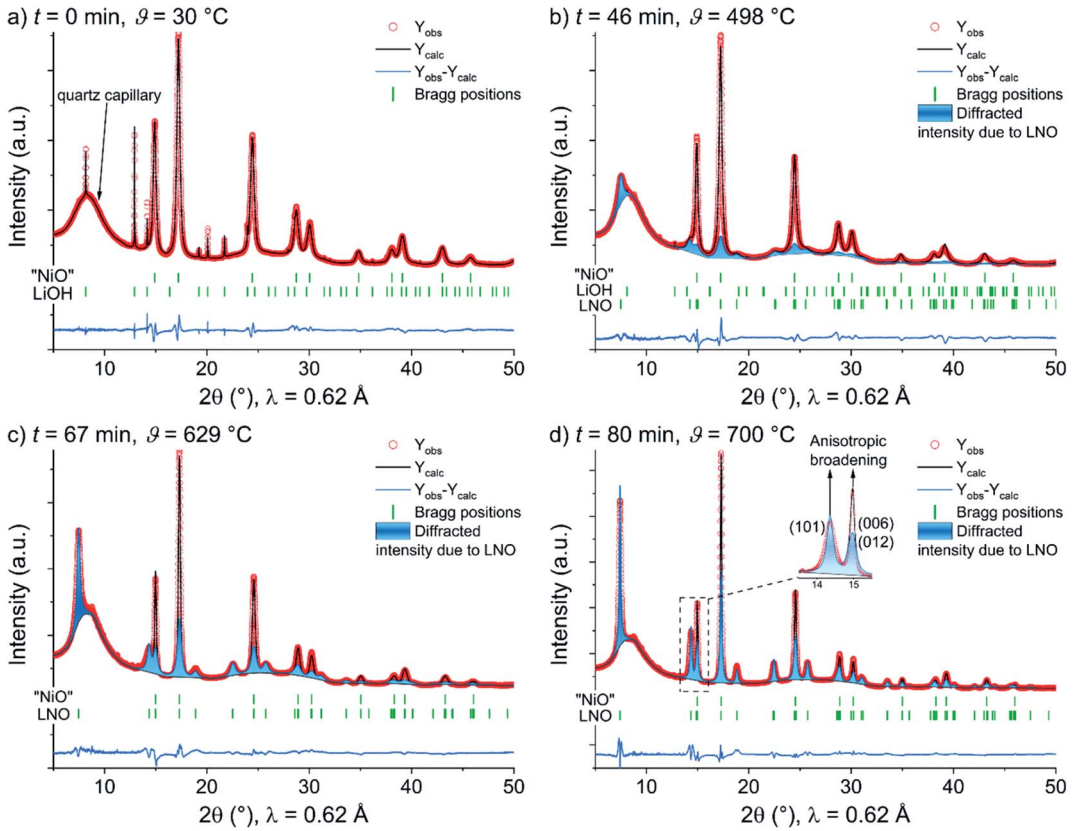

Fig. 4 Rietveld refinement of selected synchrotron X-ray diffraction patterns collected during *in situ* synthesis of LNO, from a mixture of NiO and LiOH precursors. The complete dataset is shown in Fig. 3. (a) Pristine powder mixture at t 0 min; (b) t 46 min, the diffracted intensity due to LNO is shown by the shaded blue area; (c) t 67 min; and (d) t 80 min. The issue of anisotropic broadening of LNO Bragg peaks during crystallization is highlighted in the inset.

In a rock salt phase, reflections are allowed if h, k, l are all even or odd. However, because of the third row of the above matrix, LNO's reflections that are directly related to the rock salt phase ones are always even, and these are found to be narrow. Conversely, reflections with odd l are broad and represent a planar spacing exclusively allowed in the rhombohedral

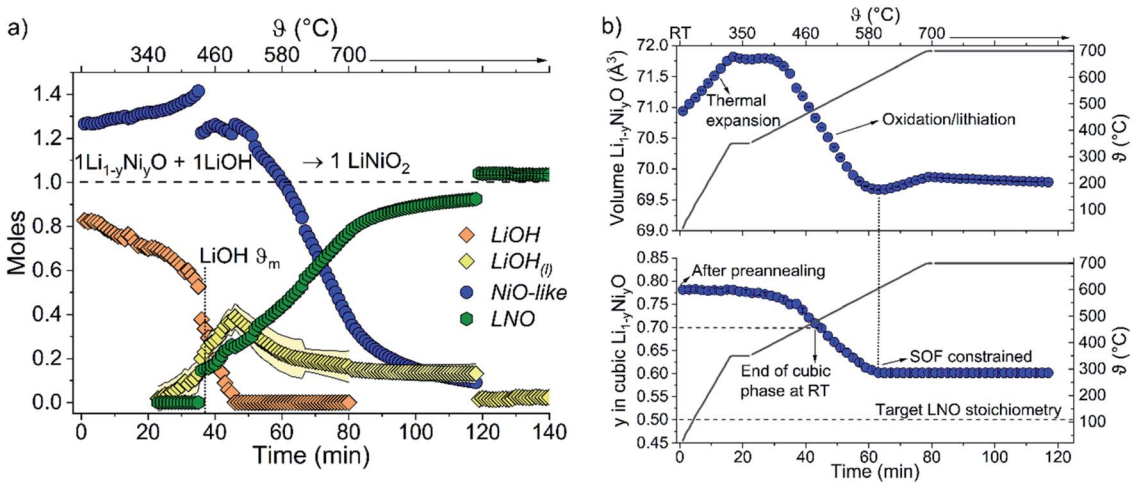

Fig. 5 Rietveld refinement of XRD data during *in situ* synthesis. Only t < 140 min is displayed, since for t > 120 min LNO is the only phase present. (a) Molar phase evolution. The values for the NiO-like phase, crystalline LiOH, and LNO are directly obtained from the values in wt% obtained from the refinement software (Fig. S7†). The value for molten LiOH was estimated from the amount of "missing" Li (Fig. S8†) as total Li (1.01 mol) minus the amount of Li found in any other phase. For all phases except $LiOH_{(l)}$, the error bars are smaller than the data points. (b) Evolution of unit cell volume and Ni site occupancy factor in the rock salt precursor $Li_{1-y}Ni_yO$. In (b) only one data point out of every two is shown for clarity.

symmetry of LNO. This explains why only the peaks that belong to LNO [*e.g.*, $(003)_R$ or $(101)_R$, not present in the parent rock salt phase] are very broad, while those also belonging to the rock salt phase [*e.g.*, $(104)_R = (002)_C$] are significantly narrower. Such an LNO-specific size broadening rule suggests that the oxygen framework is perfectly maintained during the synthesis. On the other hand, defects in LNO's layering are present during synthesis and are not relieved until higher calcination temperatures are attained. The exact nature of these defects is under investigation and out of scope of the present work. However, we believe it may be the result of specific staking faults, already observed in deintercalated LNO and $Ni(OH)_2$ samples [but mostly affecting $(10l)$ reflections in those cases][32 34] and anti-phase boundaries between adjacent LNO nanodomains. Anti-phase boundaries typically affect reflections with specific rules by influencing their intensity and shape, but not the integrated intensity.[35]

Fig. 5a gathers the evolution of each crystalline phase and the estimated content of liquid LiOH. We first observe that, during heating even at temperatures significantly lower than its melting point, the amount of LiOH decreases, while the one of $Li_{1-y}Ni_yO$ increases. This suggests that some lithium is incorporated into the cubic lattice at low temperature already. Indeed, the precursors $LiOH \cdot H_2O$ and $Ni(OH)_2$ have been pre-annealed at 350 °C and, in addition to releasing water, partial lithiation of NiO ($Li_{1-y}Ni_yO$) took place. The unit cell parameter of a reference NiO ($a = 4.1791(2)$ Å) that we prepared from $Ni(OH)_2$ differs significantly from our precursor after the initial temperature treatment in the presence of LiOH ($a = 4.1344(2)$ Å; see Fig. S1†). The lower value is consistent with lithiated NiO samples reported in literature, and one can estimate the Li content by exploiting the fact that it linearly correlates with the unit cell volume ($V_{LNO} = 3/2V_{NiO} = 101.65(5) + 7.94(10)z$ Å^3 in $Li_{1-z}Ni_{1+z}O_2$).[1] This fact, corroborated by the refinement of the Ni site occupancy factor, suggests a stoichiometry of our precursor rock salt-like phase of $Li_{0.219(5)}Ni_{0.781(5)}O$. Thus, a pre-annealing step at 350 °C for 12 h does not simply dehydrate the precursors, but it also leads to a significant amount of Li/Ni intermixing. One should note that in our analysis we refine the site-occupancy factor for nickel (SOF_{Ni}) and constrain the site to be fully occupied according to $Li_{1-y}Ni_yO$. In fact, using XRD we are sensitive only to the presence of Ni, but cannot distinguish Li from possible Ni vacancies. *A priori*, a composition $Li_{1-x-y}\square_xNi_yO$ should be considered. However, the perfect agreement between stoichiometry obtained *via* SOF refinement and *via* its relation with the unit cell volume suggests that, at this stage, the vacancy concentration in the rock salt phase is negligible. The relative molar amounts of cubic and LiOH phases at the beginning of the *in situ* experiment obtained from refinement (1.27(2) and 0.83(3) respectively; see Fig. 5a) are also in agreement with those expected from the refined amount of Ni and Li found in the cubic phase: $1.28Li_{0.22}Ni_{0.78}O + 0.73LiOH$.

Fig. 5b shows the behavior of the precursor cubic phase as the temperature increases. After a thermal expansion region, the unit cell parameter starts to decrease, in line with the expected behavior during lithiation and oxidation. The decreasing SOF_{Ni} also supports this. In literature, it is reported that the $Li_{0.3}Ni_{0.7}O$ phase has the highest lithium content allowing the existence of a cubic lattice;[1] higher Li content induces the rhombohedral distortion. Here, we observe that the SOF_{Ni} continuously decreases until the composition $Li_{0.40(1)}Ni_{0.60(1)}O$ is reached, after which the unit cell volume of the cubic phase stops decreasing, thus the SOF_{Ni} is fixed thereafter in the refinement. The observed higher lithium content in the rock salt phase may be due to several factors. Firstly, $Li_{0.3}Ni_{0.7}O$ is the limiting composition at room temperature (RT), while here we observe the phase *in situ* at temperatures up to 700 °C; it is very likely that the Li/Ni miscibility increases with increasing temperature (see for example Das *et al.*[12]). Moreover, as previously mentioned, we assume a $Li_{1-y}Ni_yO$ zero-vacancy, but some of the lithium ions could be in reality a Ni vacancy (□). If Li is replaced by a vacant site, the refinement gives a composition $\square_{0.38(1)}Ni_{0.62(1)}O$, so a large amount of vacancies may, in principle, be present (although such composition would yield an unreasonably high Ni oxidation state). Since our pristine precursor already had the

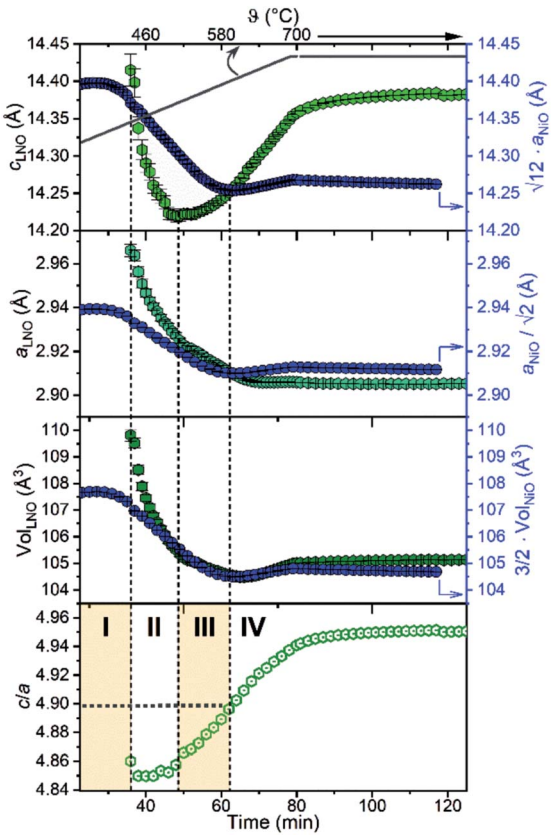

Fig. 6 Evolution of unit cell parameters, unit cell volume, and *c*/*a* ratio for $LiNiO_2$ (left axis, symbols in green) as obtained from Rietveld refinement. On the right axis, the same values are reported for the rock salt $Li_{1-y}Ni_yO$ precursor phase (symbols in blue), scaled to the appropriate values necessary because of the different unit cell choice. The division of the synthesis in 4 regions is highlighted at the bottom. The temperature profile while heating to 700 °C is also shown as grey line. Only one data point out of every two is displayed for clarity.

composition $Li_{0.219(5)}Ni_{0.781(5)}O$ and a negligible content of Ni vacancies, and $Li_{0.3}Ni_{0.7}O$ can be reached even at room temperature, it is likely that the true composition at this stage is $Li_{0.4-\delta}\square_{\delta}Ni_{0.6}O$ with $\delta < 0.08$.

The $(003)_R$ Bragg peak of a rhombohedral phase makes its appearance at $\vartheta = 436$ °C (Fig. 5). From the point of view of the refinement, we can treat the cubic–rhombohedral transition as a first order two-phase reaction, although all peaks of the cubic phase also belong to (and overlap with) the rhombohedral ones, making the phase transition somehow poorly defined. Fig. 6 reports the evolution of unit cell parameters and volume of the layered $LiNiO_2$ being formed and compares them with the values of the parent cubic phase (corrected for the different choice of unit cell).

To describe the formation of LNO, we divide the synthesis into 4 regions.

(1) Region I: rock salt phase (350 °C $\leq \vartheta <$ 436 °C, $t <$ 36 min)

LNO has not appeared yet; the behavior of the rock salt phase is described above. LiOH is present as a crystalline phase but reacting slowly with the cubic $Li_{1-y}Ni_yO$ until composition $Li_{0.25}Ni_{0.75}O$ is reached *via* oxygen and lithium incorporation.

(2) Region II: appearance of "defect" LNO, a layered phase with low c/a ratio (436 °C $\leq \vartheta <$ 517 °C, 36 $\leq t <$ 49 min)

The Bragg peaks of LNO appear, very broad at first (see (003) in particular; Fig. 3). The onset for the melting of LiOH is reached, so the phase fraction of the (crystalline) hydroxide rapidly vanishes. The unit cell parameter of the cubic phase decreases continuously, and so does SOF_{Ni}. Regarding LNO, it initially has large a and c unit cell parameters and both decrease swiftly. Most interestingly, c/a is significantly lower than the value of a perfect cubic structure ($\sqrt{6} \approx 4.9$). This is peculiar because the rhombohedral distortion always increases the c/a ratio for LNO ($\approx$4.93), LCO ($LiCoO_2$, $c/a \approx 4.99$) and related compounds. Note that this is not a temperature-induced effect (c expands more than a, so thermal effects would increase c/a, not reduce it; see the decomposition section). We will discuss the nature of this anomalous c/a ratio in the following.

(3) Region III: layered phase with increasing c/a ratio (517 °C $\leq \vartheta <$ 604 °C, 49 $\leq t <$ 63 min)

Although c/a is still < 4.9, the c unit cell parameter has reached its minimum value and starts increasing. While c increases and a decreases (this is now the expected behavior for layering of LNO), both unit cell parameters converge towards the values of the rock salt phase. This result indicates that the structural difference is only in the arrangement of Ni and Li. At this stage, LiOH is liquid and not detectable anymore by XRD, but likely it is still present and wetting the particle's surface. In fact, the SOF_{Ni} in the rock salt phase is still decreasing, eventually reaching $Li_{0.4}Ni_{0.6}O$.

(4) Region IV: evolution of regular LNO (604 °C $\leq \vartheta <$ 700 °C and annealing, 63 $\leq t <$ 120 min)

LiOH is fully consumed. The cubic phase's unit cell volume is not decreasing anymore and its SOF_{Ni} is thus being fixed in the refinement. LNO has now clearly a larger unit cell volume and c/a ratio than the rock salt phase. It is mostly a layered structure with sufficient layering to result in an elongated rhombohedral cell. From this region on, the structure of LNO is similar to that described in literature.

To gain further insight into the behavior of the anomalous LNO, we looked beyond the unit cell parameters. The quality of our synchrotron XRD data also allows for refinement of the oxygen z_{ox} atomic coordinate (Fig. S9†), of Ni SOF in both Li and Ni site, and of size and strain parameters obtained from the broadening of Bragg peaks. These results are displayed in Fig. 7. Using z_{ox}, the thickness of Ni layer (or slab, S) and Li interlayer (interslab, *I*) can be calculated as $S = (2/3 \quad 2z_{ox})c$ and $I = (c/3 \quad S)$. In LNO, typical values are $S \approx 2.11$ Å and $I \approx 2.62$ Å.[36] During the course of the synthesis, a large change of S and I can be observed in LNO (Fig. 7a), while the thickness of a "layer" in the rock salt structure changes very little. S is initially very small and

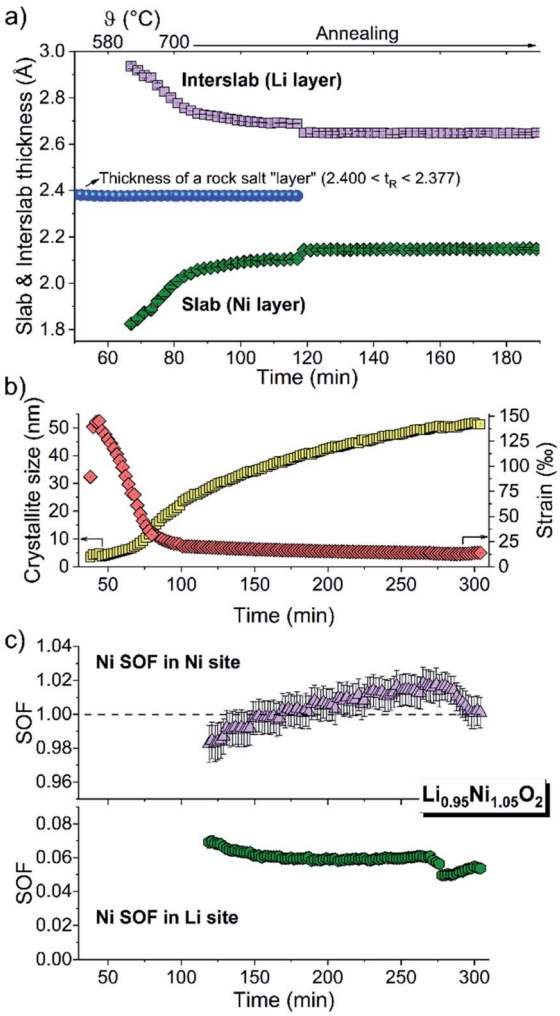

Fig. 7 (a) Evolution of thickness of Ni slab S and Li interslab I in $LiNiO_2$ compared to the thickness of a "layer" of the rock salt structure (distance between two triangular faces of an octahedron). (b) Estimated crystallite size and strain (local variation of lattice planes $\Delta d/d$) obtained from isotropic size and strain broadening contributions to the Bragg peaks during crystal growth. (c) Site occupancy factors of Ni in both the Ni and the Li layer (off-stoichiometry). The resulting composition of LNO is $Li_{0.95}Ni_{1.05}O_2$. Only one data point out of every two is displayed for clarity.

I rather large, and they converge to the expected values for LNO over time. Note that, since $I = c/3$ S, S and I are interrelated by definition, and only one mechanism is needed to explain their evolution. We believe that this is a result of the formation and agglomeration of Ni vacancies in the Ni slab S. Indeed, in our picture there is nothing larger than Li that could enlarge I. On the other hand, vacancies could be responsible for decreasing S below the size it would have when purely composed of Ni^{3+}. This finding suggests a key role of point defects and especially Ni vacancies during crystallization of LNO. As discussed later, the creation of Ni vacancies is likely the result of O and Li incorporation into the material's particles.

The fact that LNO forms as a highly defective structure is also confirmed by the size and strain parameters derived from Rietveld refinement, as shown in Fig. 7b. We initially observe coherent diffracting domains of roughly 3 nm, growing during the course of the experiment to about 50 nm. More importantly, the strain obtained in the initial XRD patterns is very high (on the order of 14%). Although the instrumental broadening has been taken into account carefully, these values should still be taken as semi-quantitative and not over-interpreted. In any case, the strain is a local deviation of d-spacing(s) from the average value(s), often caused by local defects. One of the possible origins are point defects, such as vacancies.

When $LiNiO_2$ is single phase (after the rock salt phase disappears), it is also possible to refine the SOF of Ni in the Li layer to verify the off-stoichiometry evolution [z in $(Li_{1-z}Ni_z)$ NiO_2]. To our surprise, the refinement procedure is stable even when the SOF of Li in the Ni site [$(Li_{1-z}Ni_z)$ $(Ni_{1-z'}Li_{z'})O_2$] is allowed to vary. However, this clearly increases error bars, and in general, it is not an accurate procedure since X-rays are mostly blind to small amounts of Li in a Ni-occupied site. Yet, the values we find are close to those expected, *i.e.*, no occupancy of Li in the Ni site ($z' \approx 0$). For the off-stoichiometry, we find a value of 0.05, corresponding to a final LNO stoichiometry of $Li_{0.95}Ni_{1.05}O_2$ (Fig. 7c). Although this off-stoichiometry is higher than those typically obtained in our laboratory synthesis (Fig. S3†) and in the best LNO samples reported in literature (z = 0.01–0.02 (ref. 1)), we find that the main cause is the reactivity of molten LiOH towards the quartz capillary, leading to more Li loss than expected due to the favorable formation of Li_4SiO_4. We describe in detail the reaction of a Li-containing phase with SiO_2 from the quartz capillary in the decomposition section below.

Our findings on the synthesis process are schematically summarized in Fig. 8. Both oxygen (eqn (4) and (5)) and lithium (eqn (5)) are initially incorporated into the NiO lattice according to the following relations (Kröger–Vink notation):

$$\frac{1}{2}O_{2(g)} = V''_{Ni} + O_O^{\times} + 2h^{\cdot} \quad (4)$$

$$2LiOH = H_2O + V''_{Ni} + O_O^{\times} + 2h^{\cdot} + 2Li \xrightarrow[Li+V''_{Ni}+h^{\cdot}\ \ Li'_{Ni}]{} H_2O + O_O^{\times} + h^{\cdot} + Li'_{Ni} + Li \quad (5)$$

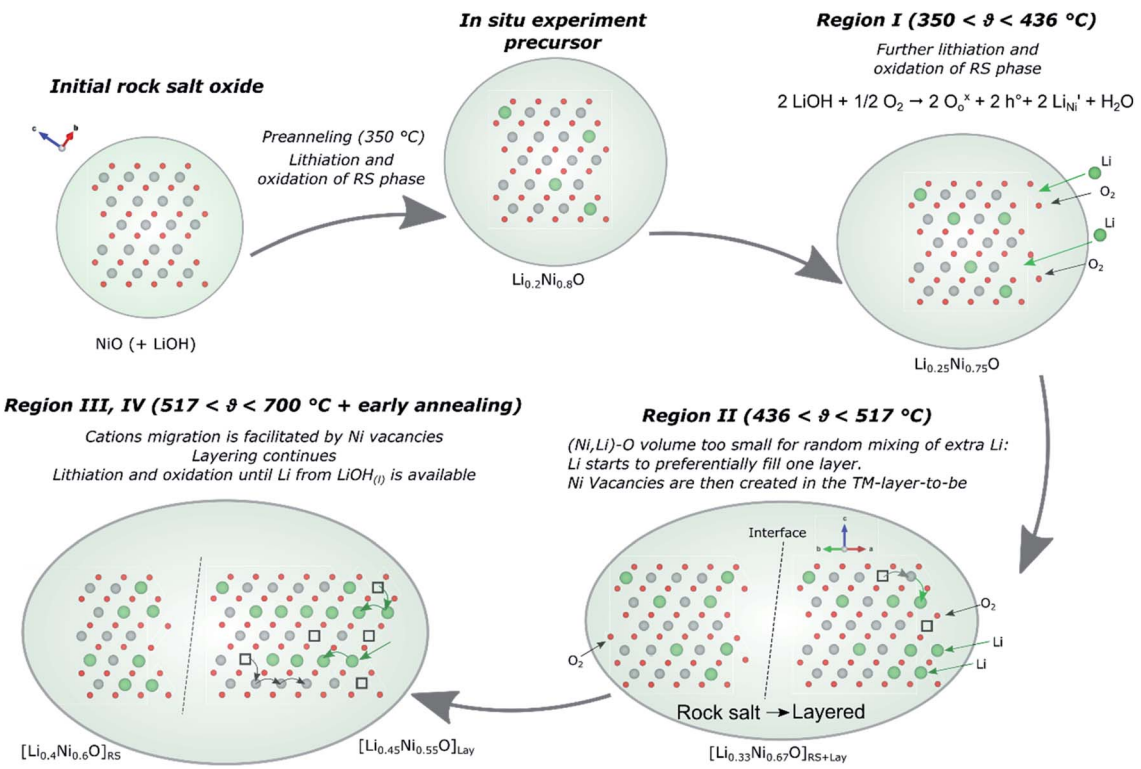

Fig. 8 Scheme summarizing the results of the *in situ* synthesis of $LiNiO_2$. Green spheres represent lithium, grey ones nickel, red ones oxygen, and squares represent vacancies. Grey and green arrows denote the movement of Ni and Li atoms, respectively. The approximate composition of the Ni-containing particles is reported below each reaction step.

The Li term in eqn (5) does not mean that elemental Li forms, but simply that not all the Li available from LiOH can react with the rock salt lattice until further O_2 from the atmosphere is also uptake (eqn (4)). Then summing up eqn (4) and (5):

$$\frac{1}{2}O_{2(g)} + 2LiOH = H_2O + 2O_O^{\times} + Li'_{Ni} + V''_{Ni} + 3h^{\cdot} + Li$$
$$= H_2O + 2O_O^{\times} + 2Li'_{Ni} + 2h^{\cdot} \quad (6)$$

and similarly to eqn (3):

$$2Ni^{2+}O + \frac{1}{2}O_{2(g)} + 2LiOH = H_2O + 2LiNi^{3+}O_2 \quad (7)$$

Hence, some Ni vacancies may form even in an early synthesis stage, although they are likely filled very quickly by lithium. These are sufficient to allow cation diffusion and yield a random arrangement of Li and Ni. As the lithium amount increases and nickel is oxidized, the unit cell volume decreases until the point where the octahedral sites are too small to be occupied randomly by further lithium, which is when layering of LNO begins. LNO initially forms as a highly defective structure, with a rhombohedral distortion that compresses the cubic structure along the [111] direction, instead of expanding it. We believe this is due to the increasing amount of vacancies in the Ni layers, compensated by very large neighboring interlayer spacing. The empty space allows Ni to migrate and cluster in slabs. On the other hand, Li diffuses fast and fills the empty sites left behind by Ni, resulting in a low vacancy content in the Li layers. As the reaction proceeds, different layered domains join and their interfaces may be incoherent in most cases, resulting in defects such as anti-phase domains and twinning, that can induce anisotropic Bragg peaks broadening in samples made at low temperature (550 °C, Fig. S6†). The final annealing interval at high temperature (700 °C) allows to heal such defects and improve the long-range periodic arrangement of atoms in crystalline LNO.

Using a Johnson–Mehl–Avrami–Kolmogorov formalism (Fig. S10 and ESI† for details) we can obtain a rough description of the LNO formation kinetics.[37] However, because the assumptions of the model include a constant temperature and the presence of only two phases, we can only apply it to the late reaction stage, after LiOH has disappeared entirely (region 4). In this region, we find that LNO crystallizes *via* a 2D growth mechanism without nucleation (Avrami exponent $n = 2$).

(II) Decomposition of $LiNiO_2$ at high temperature

Several authors attempted to optimize the solid-state synthesis of $LiNiO_2$ to obtain stoichiometric material.[1,38,40] From these studies, it became clear that even if LNO were to form with perfect stoichiometry during synthesis, it would not be stable under the high-temperature conditions and thus slowly decompose back towards a rock salt phase. As described by eqn (1), the decomposition products are $Li_{1-z}Ni_{1+z}O_2$, Li_2O, and O_2, the first being a rock salt-like phase that may not be homogeneously distributed across the sample (*i.e.*, typically z may be larger at the surface than in the bulk). The pace and extent of this transformation is strongly affected by annealing temperature, duration, and atmosphere or, in other words, by the oxygen chemical potential $\mu(O_2)$.

McCalla *et al.*[20] reported from TGA that, regardless of the gas employed, the decomposition already occurs at 700 °C, the typical synthesis temperature of LNO (Fig. 9a). It does not occur at 600 °C, while it proceeds quickly at 800 °C. Moreover, the decomposition occurs more rapidly in Ar atmosphere and significantly slower in air and in O_2. The authors also confirmed the presence of Li_2O by XRD after the TGA experiment, but only when an Ar atmosphere is used (if O_2 is present, Li_2O reacts to form Li_2O_2, which is volatile).

Here, we investigate the decomposition reaction *in situ* by synchrotron XRD in air to obtain quantitative information regarding the kinetics and extent of decomposition. The applied temperature profile is similar to the one of McCalla *et al.* and is reported in Fig. 9b. We added holds at 500 °C where the oxygen

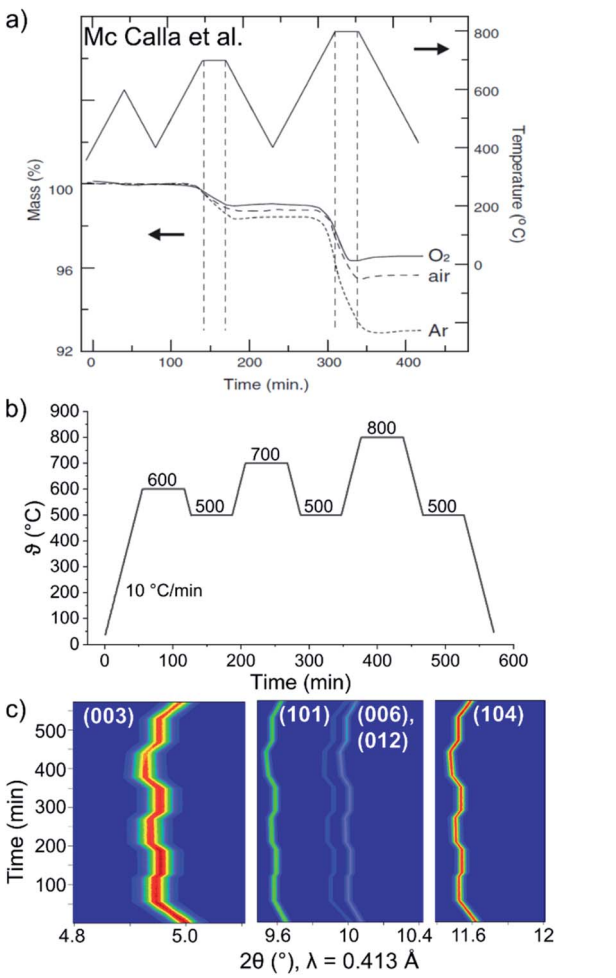

Fig. 9 (a) TGA data for $Li_{0.965}Ni_{1.035}O_2$ heated in oxygen (solid line), air (dashed line), and argon (short dashed line). A gas flow of 50 mL min ^{1} was used in each case. The vertical dashed lines mark the start and end of the temperature holds. Reproduced from McCalla *et al.*,[20] Copyright 2012, with permission from Elsevier. (b) Temperature profile used in the *in situ* XRD decomposition experiment of $Li_{0.98}Ni_{1.02}O_2$. (c) Zigzag behavior of selected LNO peaks due to thermal expansion/contraction.

chemical potential is higher to verify possible recovery of the material after decomposition at higher temperatures. Fig. 9c shows the typical evolution of selected LNO Bragg peaks. The zigzag behavior is expected and mostly due to thermal expansion/contraction effects (see also Fig. 10a–c). However, during the 700 °C and 800 °C temperature holds, irreversible changes in Bragg peak positions can be noticed, indicative of irreversible changes in crystal structure. To study such changes in detail, Rietveld analysis of XRD data was performed. Specifically, we refined throughout unit cell parameters, oxygen fractional atomic coordinate z_{ox}, isotropic Debye–Waller factors for each atom [B_{iso}(Ni), B_{iso}(Li), B_{iso}(O)], SOF of Ni on the Li site ($SOF_{Ni} + SOF_{Li} = 1$), and finally peak broadening parameters (U, X, Y). The main structural results are shown in Fig. 10.

We first observe that, as expected, the unit cell volume of LNO is constant at 600 °C, while it increases during the decomposition process at 700 °C and 800 °C. At the former temperature, the process is more than 3 times slower than at the latter. By looking at the unit cell parameters, one notices that the volume increase is mainly due to the change in a, which increases substantially. On the other hand, c barely varies at 700 °C and only slightly decreases at 800 °C, indicating minor changes in interlayer spacing. Thus, the decomposition process affects a in a stronger way than c. This can be understood by the fact that the increase in a mostly reflects the reduction of Ni^{3+} to larger Ni^{2+} in the Ni layer; c results from the interplay between Ni reduction (increase in c) and Li loss, with Ni^{2+} occupying the interslab space in place of larger Li^{+} (decrease in c). These competing effects, combined with the fact that c is strongly enlarged by thermal expansion, result in the small total variation of c. Nonetheless, when returning to room temperature, c (as well as a) is permanently enlarged by the decomposition process.

One can also notice that the thermal expansion of LNO is anisotropic: c is more affected than a ($\Delta c/c \approx 2\Delta a/a$). This also indicates that at high temperature the unit cell of LNO is elongated, as confirmed by the increased c/a ratio. c/a is a good indicator of the degree of layering in the material. The closer to 4.9, the more cubic (instead of rhombohedral) is the structure. Indeed, we observe a decrease in c/a at 700 °C and a much faster one at 800 °C, ultimately leading to an overall decrease of c/a from 4.934 to 4.929 (Fig. 10d). This observation confirms that

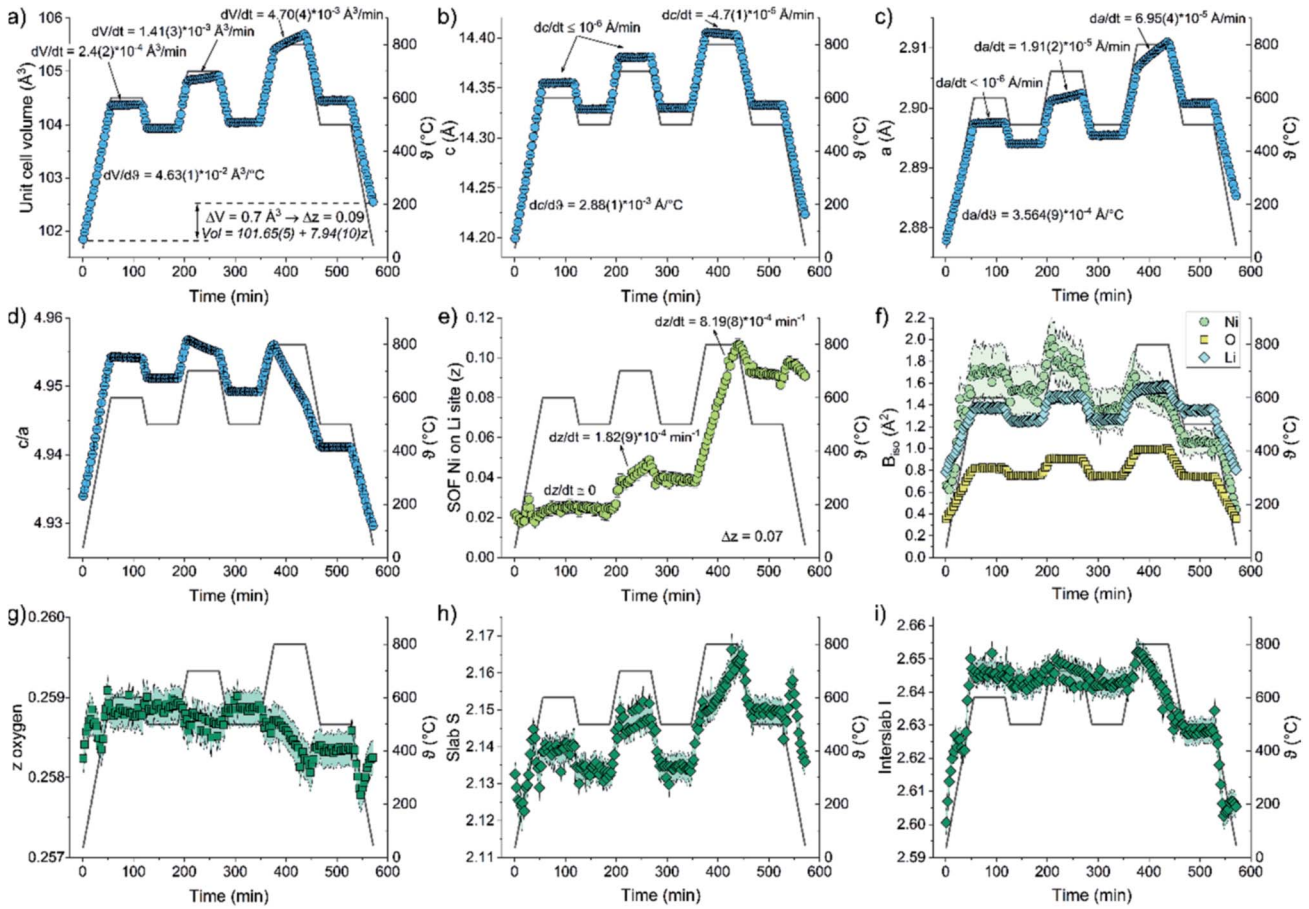

Fig. 10 Results obtained from Rietveld refinement of synchrotron XRD data for $Li_{0.98}Ni_{1.02}O_2$ as a function of temperature (grey line referring to the right axis). Only one data point out of every three is displayed for clarity. (a–d) Unit cell volume, a and c lattice parameters, and c/a ratio. Values of thermal expansion $(d/d\vartheta)_{0<t<600min}$ are given as well as the derivatives expressing the change in parameters over time at a given temperature $(d/dt)_{\vartheta\ 600°C}$, $(d/dt)_{\vartheta\ 700°C}$, and $(d/dt)_{\vartheta\ 800°C}$. (e) Site occupancy factor of Ni in the Li site (off-stoichiometry z). (f) Isotropic Debye–Waller factors B_{iso}. (g) Fractional atomic coordinate of oxygen z_{ox}. (h and i) Thickness of Ni slab S and Li interslab I.

the decomposition process is irreversible and goes in the direction of forming a structure exhibiting a less pronounced rhombohedral distortion.

By using the known linear relationship between unit cell volume and off-stoichiometry z in LNO ($V = 101.65(5) + 7.94(10)\ z$ (ref. 1)), one can estimate the total variation $\Delta z = 0.09$, *i.e.*, a final stoichiometry after the experiment of $[Li_{0.89}Ni_{0.11}]NiO_2$. On the other hand, we can obtain this value directly by refining the SOF_{Ni} of Ni cations occupying the Li site (Fig. 10e) while constraining the full site occupancy. We clearly see that z varies at 700 °C and more so at 800 °C, while there is no variation at 600 °C. Interestingly, we also observe a small recovery (decrease in z) during the cooling intervals, but not during the temperature holds at 500 °C. An overall $\Delta z = 0.07(1)$ is found from the SOF_{Ni}, which is in fair agreement with the value derived from ΔV. A possible source of mismatch comes from the fact that such decomposition at high temperature could involve also a small degree of pure Ni/Li mixing (*i.e.*, Li migrating to the Ni site), as this phenomenon is possible in strongly off-stoichiometric compounds,[36] but different probes such as neutrons should be used to verify this possibility. One can also look for direct correlations between off-stoichiometry z and values such as unit cell volume or c/a. As one might expect, a linear decrease in c/a and linear increase in volume are observed as a function of increasing z (Fig. S11†). The rate of change of both parameters is affected by the temperature, *e.g.*, the slope of the volume–z relation decreases with increasing temperature.

The refinement of Debye–Waller factors (Fig. 10f) leads to expected values in the pristine compound, *i.e.*, $B_{iso}(Ni) < B_{iso}(O) \approx B_{iso}(Li)$. Despite the large error bars for $B_{iso}(Li)$, one can still observe that such value significantly increases at high temperature, indicating high Li mobility around its average location. Interestingly, when the temperature is raised to 800 °C, $B_{iso}(Li)$ starts to decrease significantly, and at the end of the measurement, its value is only slightly larger than $B_{iso}(Ni)$. This can be understood by the fact that Ni cations migrate to the Li site, thereby lowering the average mobility of the atom occupying that site (B_{iso} is the same for Li and Ni if they occupy the same site; it only differs when they are on different sites).

Fig. 10g–i reports the evolution of slab and interslab thicknesses during the experiment, which can be calculated thanks to the refinement of the oxygen z_{ox} coordinate. Note that z_{ox} barely undergoes any changes. Since the unit cell parameter $c = 3(S + I)$ increases during the experiment, either S or I or both should increase. In our case, we observe that the slab thickness S clearly increases during the decomposition. Such increase is sufficient to account for the change in c, thus a negligible variation of the Li interslab thickness is observed. We believe this behavior is due to the fact that the increase in S can be directly related to the reduction of Ni^{3+} to Ni^{2+}, while the behavior of I is due to a more complex interplay of steric and coulombic effects.

Eqn (1) describes the decomposition of LNO. The above results clearly support the increase of z in off-stoichiometric $Li_{1-z}Ni_{1+z}O_2$ not only at the material's surface, but at the bulk level as observed by XRD. A spatially inhomogeneous distribution of z leading to a full rock salt phase at the surface is also possible (and likely), but not observable by XRD. Eqn (1) can also be confirmed by a separate observation. When $\vartheta = 700$ °C is reached during the decomposition experiment, additional peaks not belonging to LNO appear (Fig. S12†). After hypothesizing that they result from reaction of LNO (or its decomposition products) with the quartz capillary, we were able to index the new peaks to the phase Li_4SiO_4 (ICSD-35169). This compound likely forms from the reaction of SiO_2 with Li_2O according to: $2Li_2O + SiO_2 \rightarrow Li_4SiO_4$, and can thus be used as indirect evidence for the presence of Li_2O leeched out of LNO during decomposition. Note that according to eqn (1), the molar ratio between $Li_{1-z}Ni_{1+z}O_2$ and Li_2O should be $1/z$ (*i.e.*, about 10 in our case). Yet, we only find 1.3 mol% Li_4SiO_4 (1.5 wt%) and 98.7 mol% LNO, corresponding to a $Li_{1-z}Ni_{1+z}O_2/Li_2O$ ratio of 38, suggesting that only a small fraction (1/4) of the Li_2O formed from LNO reacts with SiO_2, while the rest is lost as Li_2O_2.

Discussion and conclusion

In this work, we investigated the structural evolution of $LiNiO_2$ (LNO) during its synthesis and decomposition. The two can be considered as opposite processes, *i.e.*, the former involving lithiation and oxidation of NiO, the latter Li loss and Ni reduction. We highlight the interrelation of the two processes, which indeed occur at the same temperature and similar time scales.

LNO is obtained from an industrially relevant nickel hydroxide precursor (*i.e.*, produced by precipitation) of practical spherical morphology. We find that a pre-annealing step at low temperature (350 °C) does not simply dehydrate the precursors and densify their mixture, but it also induces significant Li solubility in the NiO phase ($Li_{0.22}Ni_{0.78}O$), which is likely beneficial for LNO crystallization. The idea of a low-temperature pre-annealing step has been previously implemented in the literature, for example at 500 °C.[41] Recently, Li *et al.* similarly reported the synthesis of LNO with a pre-annealing step at 485 °C, above the LiOH melting point, to maximize the precursors homogeneity.[42] In general, such studies, in line with ours, confirm the importance of a pre-annealing step to obtain uniform and near-stoichiometric LNO. Here, we show that even lower temperatures can be used, allowing to reduce the synthesis cost and to leave the secondary particles in the precursor mixture well separated (as opposed to heating above the melting point of LiOH, which yields a ceramic product that may need manual grinding, also depending on the pre-annealing step duration, and may thus be hardly scalable).

LNO nucleation and growth are found to be rather complex processes, involving distinct structural steps already before reaching the chosen annealing temperature. Surprisingly, the rhombohedral unit cell is initially compressed, rather than elongated ($c/a < 4.9$), with respect to the cubic parent cell. Only subsequently, it evolves towards the expected LNO unit cell. The origin of the behavior of this "anomalous" LNO is rooted in the defect chemistry leading to its crystallization. Initially, we find a remarkably low value for the Ni slab thickness, which we believe is related to a significant content of Ni vacancies in the

Ni slab during the initial crystallization steps. Li and Ni migration then occur and such Ni vacancies are relieved, while the two elements segregate in two distinct layers that lower steric constraints.

On the contrary, decomposition occurs only at and above 700 °C in air. The unit cell volume decrease, correlated with the refinement of SOF_{Ni}, shows that already $\Delta z = 0.02$ is lost in just one hour at 700 °C, while $\Delta z = 0.05$ at 800 °C. The change in unit cell parameters mostly reflects in a significant change in Ni slab thickness, while it barely affects the Li interslab. Although in pure oxygen one would expect a slightly slower decomposition rate, our observation confirms that the synthesis of LNO is intrinsically problematic, as the chosen synthesis conditions must be fruit of compromise to avoid decomposition. A calcination step close to 700 °C is needed to annihilate most defects within the crystal structure, yet rather short annealing times at 700 °C should be preferred, or the annealing temperature should be decreased towards 650 °C.

In conclusion, we believe the insight provided here may be of help in optimizing the synthesis of LNO samples while minimizing decomposition effects. Furthermore, such understanding can be seen as a starting point to study new Ni-rich compositions. When targeting compounds with ≥95% Ni content, the amount of elemental substitution is low and thus the similarity to LNO high, yet the presence of specific foreign cations can facilitate the preparation of samples with improved structural stability. Our work may then serve as a first step towards understanding, improving, and optimizing the synthesis of such doped LNO samples.

Conflicts of interest

There are no conflicts to declare.

Acknowledgements

This study is part of the projects being funded within the BASF International Network for batteries and electrochemistry. The authors acknowledge MSPD and the ALBA synchrotron for the beamtime awarded under proposal 2018093026. Aleksandr Missiul is acknowledged for help in using the flow cell setup, Simon Schweidler and David Kitsche for support during beamtime, as well as Maria Roca-Ayats for support with TGA data.

Notes and references

1 M. Bianchini, M. Roca-Ayats, P. Hartmann, T. Brezesinski and J. Janek, *Angew. Chem., Int. Ed.*, 2018, 10434–10458, DOI: 10.1002/anie.201812472.
2 J. R. Dahn, U. Vonsacken and C. A. Michal, *Solid State Ionics*, 1990, **44**, 87–97.
3 S.-T. Myung, F. Maglia, K.-J. Park, C. S. Yoon, P. Lamp, S.-J. Kim and Y.-K. Sun, *ACS Energy Lett.*, 2017, **2**, 196–223.
4 A. Manthiram, B. Song and W. Li, *Energy Storage Materials*, 2017, **6**, 125–139.
5 H. Li, M. Cormier, N. Zhang, J. Inglis, J. Li and J. R. Dahn, *J. Electrochem. Soc.*, 2019, **166**, A429–A439.
6 U. H. Kim, D. W. Jun, K. J. Park, Q. Zhang, P. Kaghazchi, D. Aurbach, D. T. Major, G. Goobes, M. Dixit, N. Leifer, C. M. Wang, P. Yan, D. Ahn, K. H. Kim, C. S. Yoon and Y. K. Sun, *Energy Environ. Sci.*, 2018, **11**, 1271–1279.
7 C. S. Yoon, U.-H. Kim, G.-T. Park, S. J. Kim, K.-H. Kim, J. Kim and Y.-K. Sun, *ACS Energy Lett.*, 2018, **3**, 1634–1639.
8 M. D. Radin, S. Hy, M. Sina, C. C. Fang, H. D. Liu, J. Vinckeviciute, M. H. Zhang, M. S. Whittingham, Y. S. Meng and A. Van der Ven, *Adv. Energy Mater.*, 2017, **7**(20), 1602888.
9 D. Andre, S.-J. Kim, P. Lamp, S. F. Lux, F. Maglia, O. Paschos and B. Stiaszny, *J. Mater. Chem. A*, 2015, **3**, 6709–6732.
10 L. de Biasi, A. O. Kondrakov, H. Geßwein, T. Brezesinski, P. Hartmann and J. Janek, *J. Phys. Chem. C*, 2017, **121**, 26163–26171.
11 R. Shannon, *Acta Crystallogr., Sect. A: Cryst. Phys., Diffr., Theor. Gen. Crystallogr.*, 1976, **32**, 751–767.
12 H. Das, A. Urban, W. Huang and G. Ceder, *Chem. Mater.*, 2017, **29**, 7840–7851.
13 R. J. Moore and J. White, *J. Mater. Sci.*, 1974, **9**, 1401–1408.
14 H. N. Migeon, M. Zanne, C. Gleitzer and J. Aubry, *J. Mater. Sci.*, 1978, **13**, 461–466.
15 L. de Biasi, A. Schiele, M. Roca-Ayats, G. Garcia, T. Brezesinski, P. Hartmann and J. Janek, *ChemSusChem*, 2019, **12**, 2240–2250.
16 C. S. Yoon, D.-W. Jun, S.-T. Myung and Y.-K. Sun, *ACS Energy Lett.*, 2017, **2**, 1150–1155.
17 F. Lin, I. M. Markus, D. Nordlund, T.-C. Weng, M. D. Asta, H. L. Xin and M. M. Doeff, *Nat. Commun.*, 2014, **5**, 3529.
18 F. Kong, C. Liang, L. Wang, Y. Zheng, S. Perananthan, R. C. Longo, J. P. Ferraris, M. Kim and K. Cho, *Adv. Energy Mater.*, 2019, **9**, 1802586.
19 T. Sata, *Ceram. Int.*, 1998, **24**, 53–59.
20 E. McCalla, G. H. Carey and J. R. Dahn, *Solid State Ionics*, 2012, **219**, 11–19.
21 D. P. Shoemaker, Y.-J. Hu, D. Y. Chung, G. J. Halder, P. J. Chupas, L. Soderholm, J. Mitchell and M. G. Kanatzidis, *Proc. Natl. Acad. Sci. U. S. A.*, 2014, **111**, 10922–10927.
22 F. Fauth, I. Peral, C. Popescu and M. Knapp, *Powder Diffr.*, 2013, **28**, S360–S370.
23 P. J. Chupas, K. W. Chapman, C. Kurtz, J. C. Hanson, P. L. Lee and C. P. Grey, *J. Appl. Crystallogr.*, 2008, **41**, 822–824.
24 H. M. Rietveld, *J. Appl. Crystallogr.*, 1969, **2**, 65.
25 M. Bianchini, F. Fauth, N. Brisset, F. Weill, E. Suard, C. Masquelier and L. Croguennec, *Chem. Mater.*, 2015, **27**, 3009–3020.
26 J. Rodriguez-Carvajal, *Physica B*, 1993, **192**, 55–69.
27 Y. M. Chiang, Y. I. Jang, H. Wang, B. Huang, D. R. Sadoway and P. Ye, *J. Electrochem. Soc.*, 1998, **145**, 887–891.
28 M. W. Chase Jr, *NIST-JANAF thermochemical tables*, American Chemical Society, American Institute of Physics for the National Institute of Standards and Technology, Washington, DC, New York, Fourth edition, 1998.

29 J. B. Goodenough, D. G. Wickham and W. J. Croft, *J. Phys. Chem. Solids*, 1958, **5**, 107–116.
30 E. Antolini, *Mater. Chem. Phys.*, 2003, **82**, 937–948.
31 S. Deng, L. Xue, Y. Li, Z. Lin, W. Li, Y. Chen, T. Lei, J. Zhu and J. Zhang, *J. Electrochem. Energy Convers. Storage*, 2019, **16**, 031004.
32 L. Croguennec, C. Pouillerie, A. N. Mansour and C. Delmas, *J. Mater. Chem.*, 2001, **11**, 131–141.
33 C. Delmas and C. Tessier, *J. Mater. Chem.*, 1997, **7**, 1439–1443.
34 C. Tessier, P. H. Haumesser, P. Bernard and C. Delmas, *J. Electrochem. Soc.*, 1999, **146**, 2059–2067.
35 B. E. Warren, *X-ray Diffraction*, Dover Books, 1990.
36 C. Pouillerie, E. Suard and C. Delmas, *J. Solid State Chem.*, 2001, **158**, 187–197.
37 M. Avrami, *J. Chem. Phys.*, 1939, **7**, 1103–1112.
38 A. Rougier, P. Gravereau and C. Delmas, *J. Electrochem. Soc.*, 1996, **143**, 1168–1175.
39 R. Kanno, H. Kubo, Y. Kawamoto, T. Kamiyama, F. Izumi, Y. Takeda and M. Takano, *J. Solid State Chem.*, 1994, **110**, 216–225.
40 H. Arai, S. Okada, H. Ohtsuka, M. Ichimura and J. Yamaki, *Solid State Ionics*, 1995, **80**, 261–269.
41 H. Arai, M. Tsuda and Y. Sakurai, *J. Power Sources*, 2000, **90**, 76–81.
42 H. Li, N. Zhang, J. Li and J. R. Dahn, *J. Electrochem. Soc.*, 2018, **165**, A2985–A2993.